Supporting Information

Manganese- and Selenium-codoping CeO_2@Co_3O_4 Porous Core-shell Nanospheres for Enhanced Oxygen Evolution Reaction

Xianggang Huang,[‡a] Xin Wang,[‡b] Mengling Zhang,[a] Qilei Jiang,[a] Zheng Qin,[a] Yingxin Liu,[a] Yan Hou,[a] Xueqin Cao[*a] and Hongwei Gu[*a]

a Key Laboratory of Organic Synthesis of Jiangsu Province, College of Chemistry, Chemical Engineering and Materials Science and Collaborative Innovation Center of Suzhou Nano Science and Technology, Soochow University, Suzhou 215123, P. R. China.

b Key Laboratory of Rare Mineral of hubei Province, Ministry of Natural Resources, Hubei Geological Experimental Testing Center, Wuhan 430034, P. R. China.

‡ These authors contributed equally.

* Corresponding authors:

E-mail: hongwei@suda.edu.cn; xqcao@suda.edu.cn.

Table of contents

3, Mn-CeO_2@Co_3O_4, CoCeMn-Oxides-5.

Figure S13 XRD pattern (a) and Magnified XRD spectra (b) of the Co-Oxides, CoCe-Oxides, CoMn-Oxides, Mn-CeO_2@Co_3O_4 and MnSe-CeO_2@Co_3O_4.

Figure S14 Nitrogen adsorption-desorption isotherms (a) and pore size distribution plot (b) of MnSe-CeO_2@Co_3O_4.

Figure S15 High-resolution XPS spectra of (a) Co 2p and (b) O 1s of Co-Oxides-Se.

Figure S16 CV curves of (a) CoCeMn-Oxides-1, (b) CoCeMn-Oxides-2, (c) CoCeMn-Oxides-3 and (d) CoCeMn-Oxides-5 with different scan rates from 10 to 60 mV s^{-1}.

Figure S17 (a) LSV polarization curves of CoCeMn-Oxides-x (x = 1-5) in 1 M KOH aqueous solution for OER. (b) Corresponding Tafel slopes. (c) The corresponding overpotentials and Tafel slopes at 10 mA cm^{-2}. (d) Double-layer capacitance (C_{dl}) obtained by linear fitting of the capacitive currents.

Figure S18 (a) LSV polarization curves of RuO_2 and MnSe-CeO_2@Co_3O_4 in 1 M KOH aqueous solution for OER.

Figure S19 (a) LSV polarization curves of Mn-CeO_2@Co_3O_4, CoCeMn-Oxides-x (x = 6-10) in 1 M KOH aqueous solution. (b) LSV polarization curves of MnSe-CeO_2@Co_3O_4, CoMn-Oxides-Se, CoCe-Oxides-Se, and Co-Oxides-Se in 1 M KOH aqueous solution.

Figure S20 CV curves of (a) Co-Oxides, (b) CoMn-Oxides, (c) CoCe-Oxides, (d) Mn-CeO_2@Co_3O_4 and (e) MnSe-CeO_2@Co_3O_4 with different scan rates from 10 to 60 mV s^{-1}.

Figure S21 LSV curves of MnSe-CeO_2@Co_3O_4 before and after 1000 cycles of CV test.

Figure S22 HRTEM image of MnSe-CeO_2@Co_3O_4 after CP test.

Figure S23 SAED pattern of MnSe-CeO_2@Co_3O_4 after CP test.

Table S1 Atomic ratio of Ce, Co, Mn and Co/Ce from ICP-AES analysis on CoCe-CDSAAs, CoMn-CDSAAs and CoCeMn-CDSAAs-x (x = 1-9).

Table S2 Atomic ratio of Ce, Co, Mn and Co/Ce from EDX analysis on CoCe-Oxides, CoMn-Oxides and CoCeMn-Oxides-x (x = 1-9).

Table S3 Atomic ratio of Co^{3+}/Co^{2+} and O2/(O1+O2+O3) from XPS analysis on Co-Oxides, CoMn-Oxides, CoCe-Oxides, Mn-CeO_2@Co_3O_4, MnSe-CeO_2@Co_3O_4, Co-Oxides-Se and MnSe-CeO_2@Co_3O_4 (After CP).

Table S4 Comparison of the OER performance of MnSe-CeO_2@Co_3O_4 with previously reported Co-based and Ce-based OER electrocatalysts.

3 Reference

1. Experimental Section

1.1 Chemicals and Materials

Manganese (Ⅱ) acetate tetrahydrate ($Mn(OAc)_2·4H_2O$), Cobalt (Ⅱ) acetate tetrahydrate ($Co(OAc)_2·4H_2O$), methanol anhydrous and selenium powder are purchased from Sinopharm Chemical Reagent Co., Ltd. Cerium (Ⅲ) acetate Sesquihydrate ($Ce(OAc)_3·xH_2O$) is purchased from Shanghai Yuanye Bio-Technology Co., Ltd. All chemicals and reagents are analytical purity and use directly without further purification.

1.2 Synthesis of CoCeMn-CDSAAs-x (x = 1-10), Co-CDSAAs, CoCe-CDSAAs and CoMn-CDSAAs

The organic ligand (Z)-4-amino-5-(hydroxyimino)-2-(4-n-octyloxyphenyl)-2,5-dihydro-1H-imidazole-3-oxide (HL_{10}) and Co-CDSAAs are prepared according to our previous report.[1] Firstly, HL_{10} (0.6 mmol, 200.1 mg) is dissolved in 50 mL methanol at 85 ℃. Then $Ce(OAc)_3·xH_2O$ (0.025 mmol, 7.93 mg) in 1mL deionized water is added and reflux at 65 ℃ for 1h, while $Mn(OAc)_2·4H_2O$ (0.1 mmol, 24.51 mg) in 5 mL methanol is added and refluxed at 65 ℃ for 1 h. Finally, $Co(OAc)_2·4H_2O$ (0.2 mmol, 49.82 mg) is added and refluxed at 65 ℃ for 12 h. The brown CoCeMn-CDSAAs (that are CoCeMn-CDSAAs-4) are obtained by centrifugation.

Meanwhile, the CoCe-CDSAAs and the CoMn-CDSAAs are prepared through the same procedure except without adding $Mn(OAc)_2·4H_2O$ (0.1 mmol, 24.51 mg) and $Ce(OAc)_3·xH_2O$ (0.025 mmol, 7.93 mg), respectively.

In addition, the CoCeMn-CDSAAs with different Ce contents can also be obtained by changing the amount of $Ce(OAc)_3·xH_2O$ (0.2 mmol, 0.1 mmol, 0.05 mmol, 0.0167 mmol) in the reaction and denoted them as CoCeMn-CDSAAs-1, CoCeMn-CDSAAs-2, CoCeMn-CDSAAs-3 and CoCeMn-CDSAAs-5 respectively. Similarly, when adjusting the amounts of $Co(OAc)_2·4H_2O$ (0.1mmol, 0.3mmol) and $Mn(OAc)_2·4H_2O$ (0.05mmol, 0.15mmol) or synthesizing by one step method, the CoCeMn-CDSAAs-x (x = 6-10) are

obtained respectively.

1.3 Synthesis of CoCeMn-Oxides-x (x = 1-10), CoCe-Oxides, CoMn-Oxides and Co-Oxides

The prepared CoCeMn-CDSAAs-x (x = 1-10), CoCe-CDSAAs, CoMn-CDSAAs and Co-CDSAAs are heated at 1 ℃ min^{-1} in the air atmosphere respectively. When the calcination temperature reach 600 ℃, the materials are kept at this temperature for 5 h. After cooling to room temperature, the black products are obtained and denote as CoCeMn-Oxides-x (x = 1-10), CoCe-Oxides, CoMn-Oxides and Co-Oxides (CoCeMn-Oxides-4 are denoted as Mn-CeO_2@Co_3O_4) respectively.

1.4 Synthesis of MnSe-CeO_2@Co_3O_4, CoCe-Oxides-Se, CoMn-Oxides-Se and Co-Oxides-Se

Se powder and Mn-CeO_2@Co_3O_4 are placed at two separate positions in a Porcelain Ark, with Se powder at the air inlet of a tube furnace and the Mn-CeO_2@Co_3O_4 at the air outlet of the tube furnace. After annealing the products at 350 ℃ for 3 h with a heating rate of 2 ℃ min^{-1} under an Ar atmosphere with a slow flow rate, the black MnSe-CeO_2@Co_3O_4 are obtained. Meanwhilie, the CoCe-Oxides-Se, CoMn-Oxides-Se and Co-Oxides-Se are obtained through the same procedure, respectively.

1.5 Material characterization

The morphologys of samples are characterized by scanning electron microscope (SEM, Hitachi S-4700), transmission electron microscope (TEM, TecnaiG220, FEI). The X-ray diffraction (XRD) patterns of synthesized catalysts are tested by X'Pert-Pro MPD diffractometer (Netherlands PANalytical) with a Cu Kα X-ray source (λ = 1.540598 Å). Fourier transform infrared spectra (FT-IR) images over a rage of 500 to 4,000 cm^{-1} are obtained by FT-IR spectrum (FT-IR, Nicolet5700 is5). Elemental analysis of C, N, O, Co, Ce, Mn and Se in the samples are detected by SEM-energy-dispersive-X-ray spectroscopy (SEM-EDX). The larger-magnified nanostructures and EDX elemental mappings are characterized using a high-resolution TEM (HRTEM, Tecnai G2 F20 S-TWIN). The metal element contents are obtained by Inductively coupled plasma

atomic emission spectrophotometer (ICP-AES, Varian 710-ES, USA). The Brunauere-Emmette-Teller (BET) and Barrett-Joyner-Halenda (BJH) models are used to analyze thespecific surface area and pore size of sample. To further analyze the surface electronic structure of the nanomaterials, X-ray photoelectron spectroscopy (XPS, Escalab250Xi, UK) is performed using a hemispherical electron energy analyzer.

1.6 Electrochemical measurements

The electrochemical measurements are performed using a three-electrode cell on a CHI660E electrochemical workstation. The Ag/AgCl electrode (KCl saturated), graphite electrode and glassy carbon (GC) disk electrode (5 mm in diameter) are used as the reference, counter and working electrodes in the three-electrode electrolytic cell respectively. Furthermore, the catalyst slurry is prepared by dispersing 5 mg catalysts, 2 mg carbon powder, and 30 µL 0.5 wt% Nafion solution in 0.97 mL isopropanol solution via an ultrasonic reaction for 25 min. Drying at room temperature, 3 µL of slurry is added to the GC electrode (diameter: 5 mm, area: 0.19635 cm^{-2}) seven times (21 µL in total) and subsequent electrochemical tests are performed. The calculated loading of the catalyst on the GC electrode is 0.53476 mg/cm^{-2}. The potentials of catalysts are referenced to a reversible hydrogen electrode (RHE) according to the Nernst equation: $E_{RHE} = E_{Ag/AgCl} + 0.197 + 0.059 \times pH$. In 1.0 M KOH solution, Linear sweep voltammetry (LSV) curves are tested at room temperature with a scan rate of 10 mV s^{-1}. All overpotential (η) values are calculated according to formula: $\eta = E_{RHE} - 1.23$ V. Chronopotentiometry test is carried out on a carbon paper (0.5 cm × 1 cm, loading of 0.4 mg cm^{-2}). In a non-faradaic region, the electrochemical double layer capacitance (C_{dl}) can be calculated from the cyclic voltammograms measured at different scan rates (v = 10, 20, 30, 40, 40, 50 and 60 mV s^{-1}). The current density difference of the half-potential at the same sweep speed against the scan rates are plotted and fitted to obtain C_{dl} values. Electrochemical impedance spectroscopy (EIS) is measured in the frequency scan range from 10^5 Hz to 10^{-2} Hz.

2. Supporting Figures and Tables

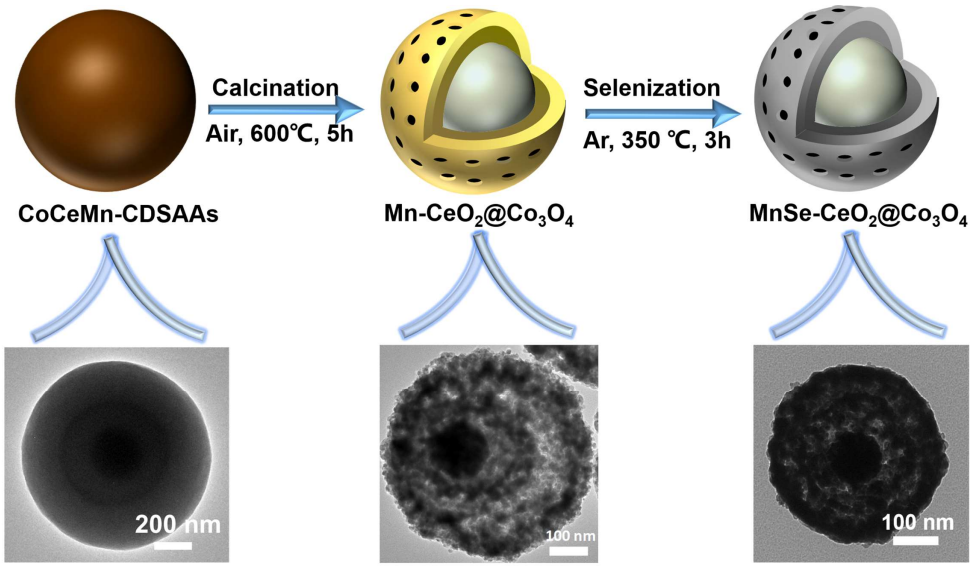

Figure S1 Schematic diagram of the structure evolution after calcination and selenization.

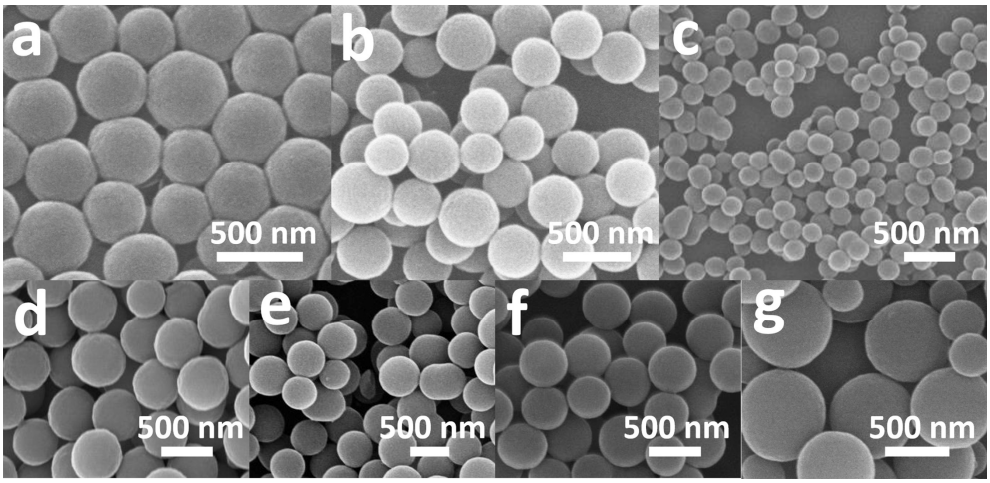

Figure S2 SEM images of (a) Co-CDSAAs, (b) CoCe-CDSAAs, (c) CoMn-CDSAAs, (d) CoCeMn-CDSAAs-1, (e) CoCeMn-CDSAAs-2, (f) CoCeMn-CDSAAs-3, (g) CoCeMn-CDSAAs-5.

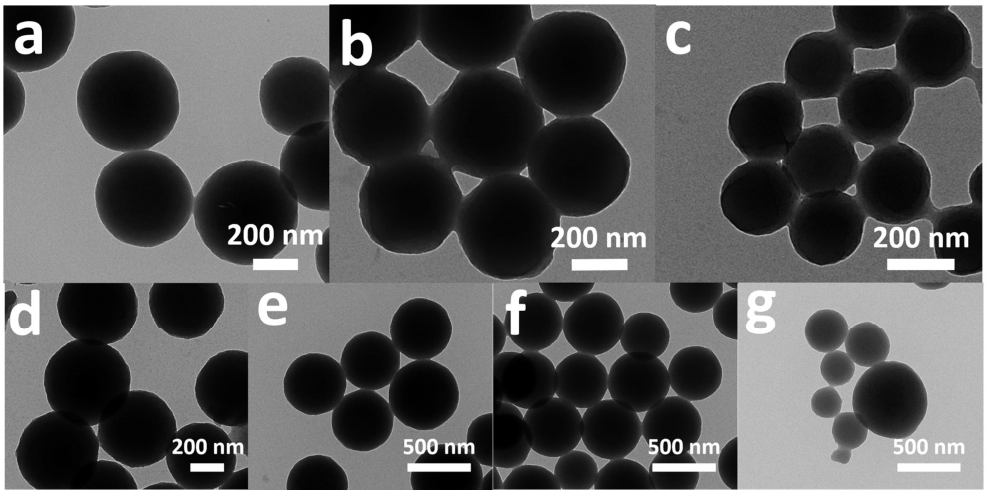

Figure S3 TEM images of (a) Co-CDSAAs, (b) CoCe-CDSAAs, (c) CoMn-CDSAAs, (d) CoCeMn-CDSAAs-1, (e) CoCeMn-CDSAAs-2, (f) CoCeMn-CDSAAs-3, (g) CoCeMn-CDSAAs-5.

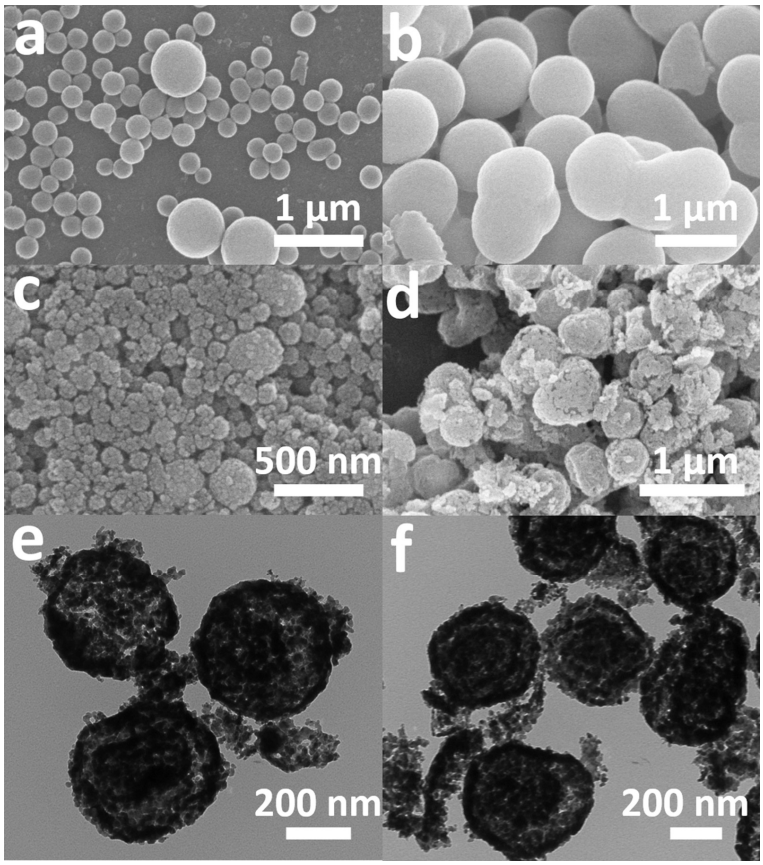

Figure S4 SEM images of (a) CoCeMn-CDSAAs-6, (b) CoCeMn-CDSAAs-7. SEM and TEM images of (c, e) CoCeMn-Oxides-6, (d, f) CoCeMn-Oxides-7.

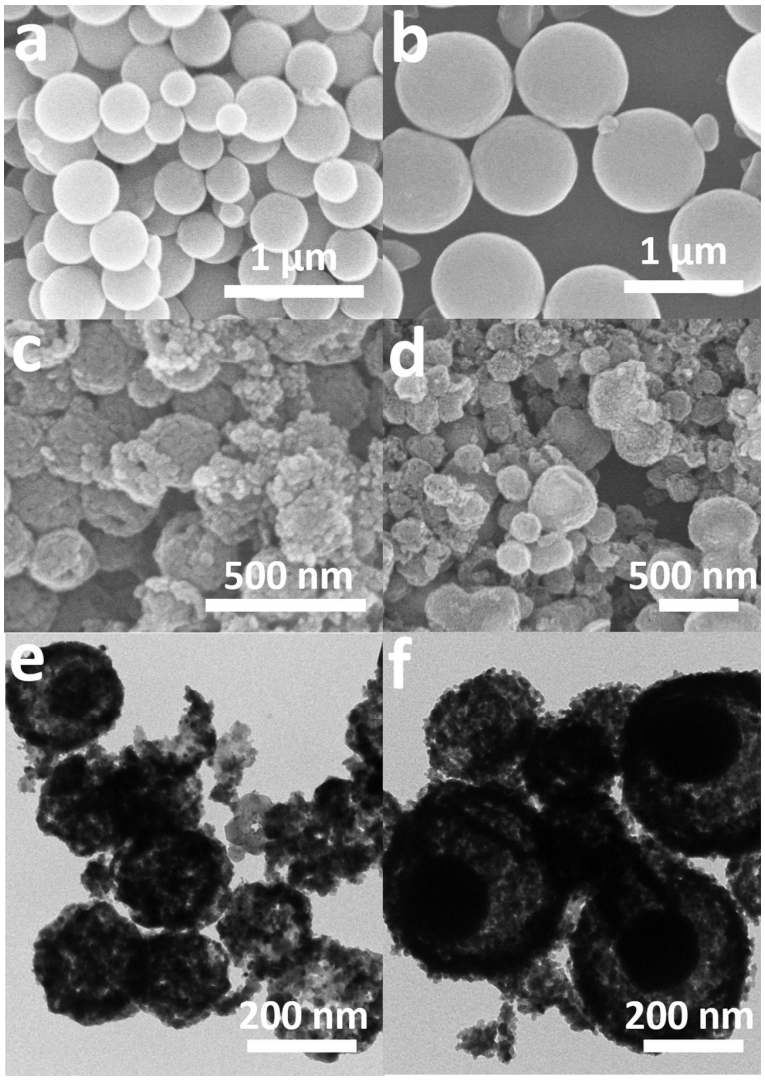

Figure S5 SEM images of (a) CoCeMn-CDSAAs-8, (b) CoCeMn-CDSAAs-9. SEM and TEM images of (c, e) CoCeMn-Oxides-8, (d, f) CoCeMn-Oxides-9.

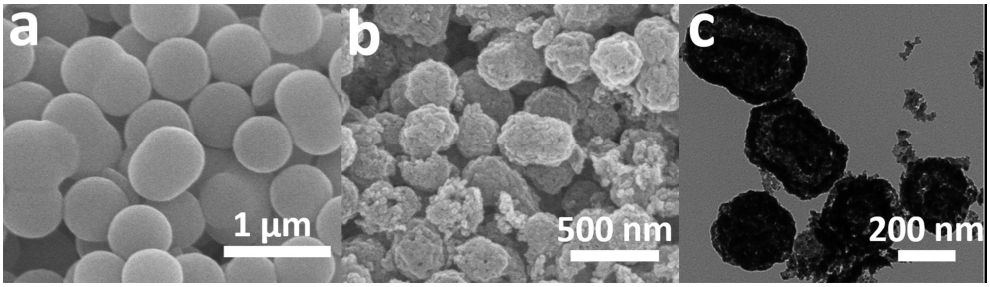

Figure S6 SEM image of (a) CoCeMn-CDSAAs-10, SEM and TEM image of (b, c) CoCeMn-Oxides-10.

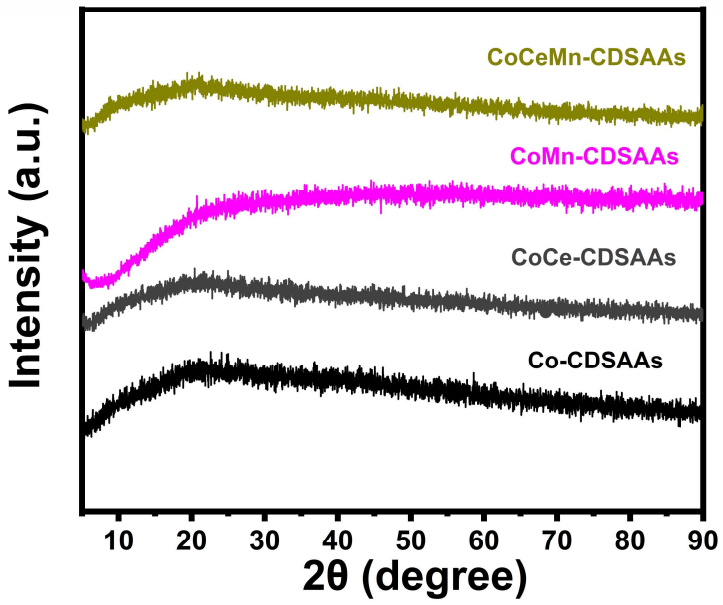

Figure S7 XRD pattern of the Co-CDSAAs, CoCe-CDSAAs, CoMn-CDSAAs, CoCeMn-CDSAAs.

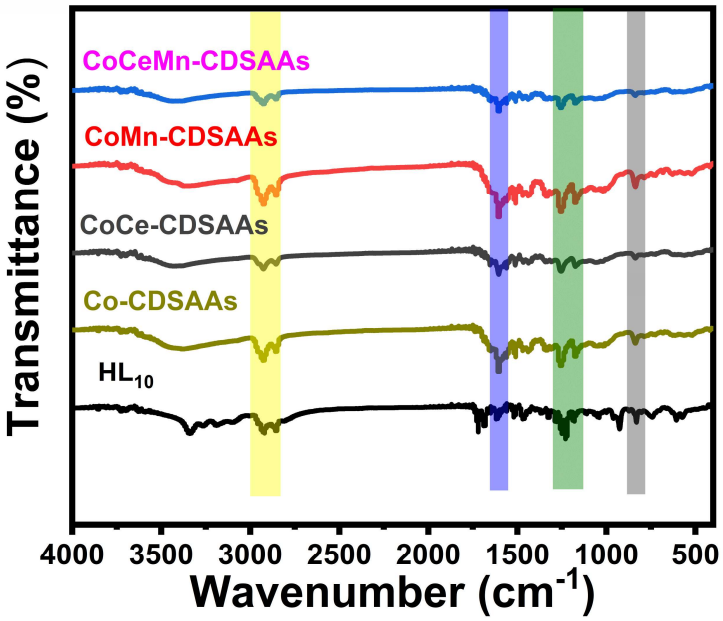

Figure S8 FT-IR spectra of the HL_{10}, Co-CDSAAs, CoCe-CDSAAs, CoMn-CDSAAs, CoCeMn-CDSAAs.

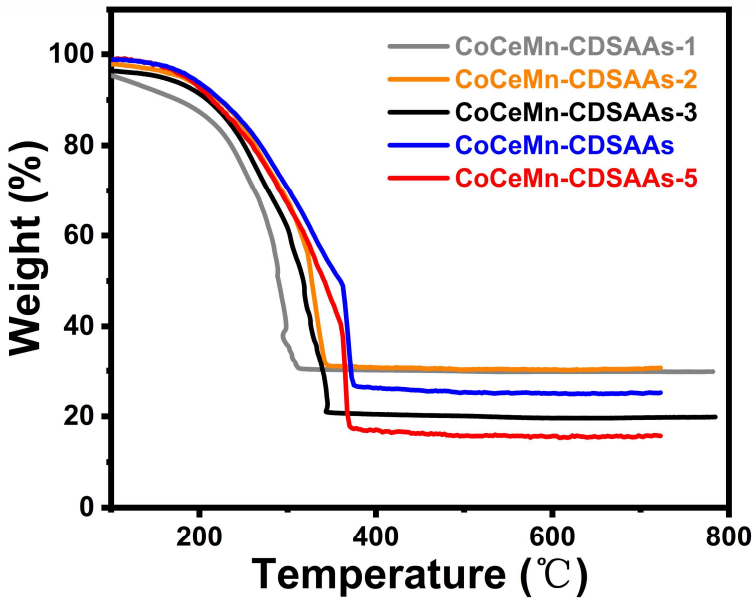

Figure S9 Thermogravimetric (TGA) curves of the CoCeMn-CDSAAs-1, CoCeMn-CDSAAs-2, CoCeMn-CDSAAs-3, CoCeMn-CDSAAs, CoCeMn-CDSAAs-5.

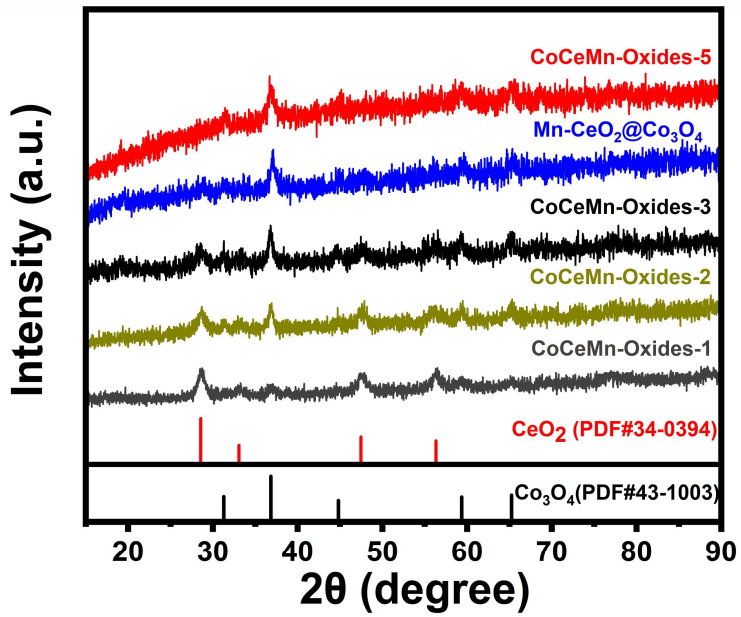

Figure S10 XRD pattern of the CoCeMn-Oxides-1, CoCeMn-Oxides-2, CoCeMn-Oxides-3, Mn-CeO_2@Co_3O_4, CoCeMn-Oxides-5.

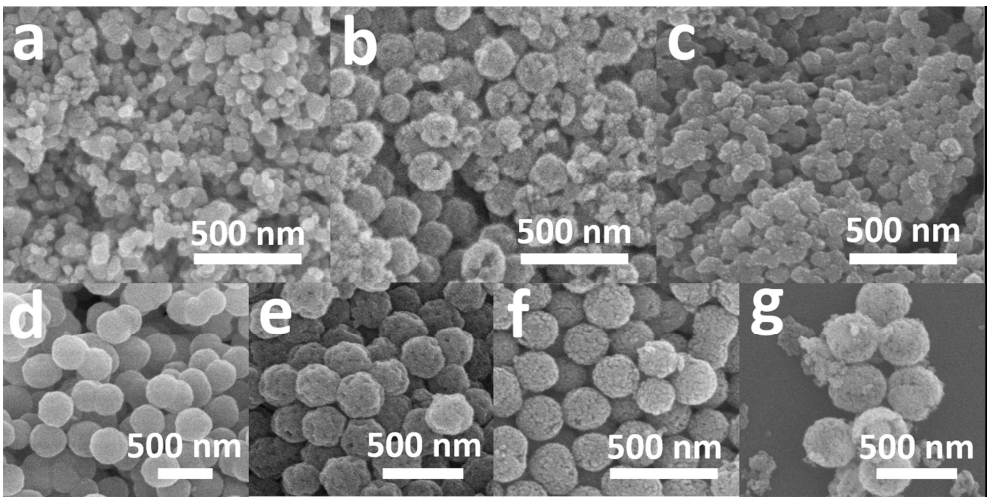

Figure S11 SEM images of the (a) Co-Oxides, (b) CoCe-Oxides, (c) CoMn-Oxides, (d) CoCeMn-Oxides-1, (e) CoCeMn-Oxides-2, (f) CoCeMn-Oxides-3, (g) CoCeMn-Oxides-5.

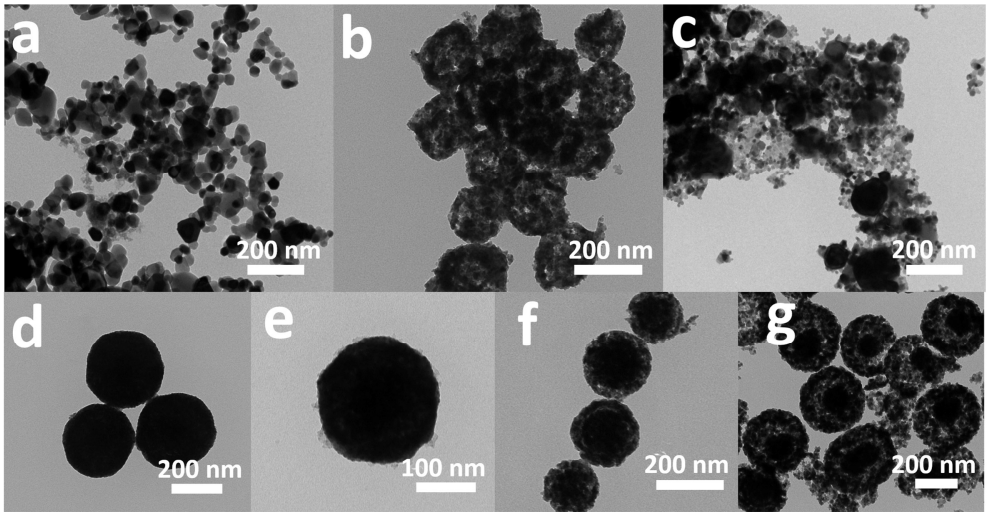

Figure S12 TEM images of the (a) Co-Oxides, (b) CoCe-Oxides, (c) CoMn-Oxides, (d) CoCeMn-Oxides-1, (e) CoCeMn-Oxides-2, (f) CoCeMn-Oxides-3, (g) CoCeMn-Oxides-5.

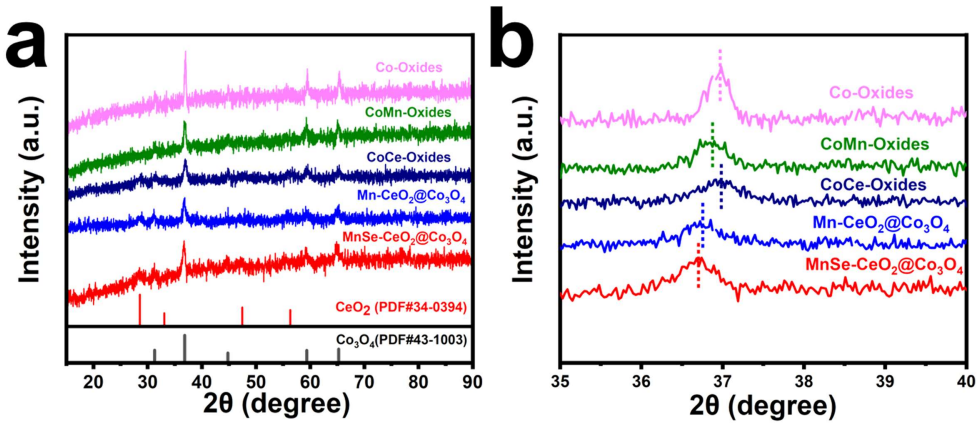

Figure S13 XRD pattern (a) and Magnified XRD spectra (b) of the Co-Oxides, CoCe-Oxides, CoMn-Oxides, Mn-CeO_2@Co_3O_4 and MnSe-CeO_2@Co_3O_4.

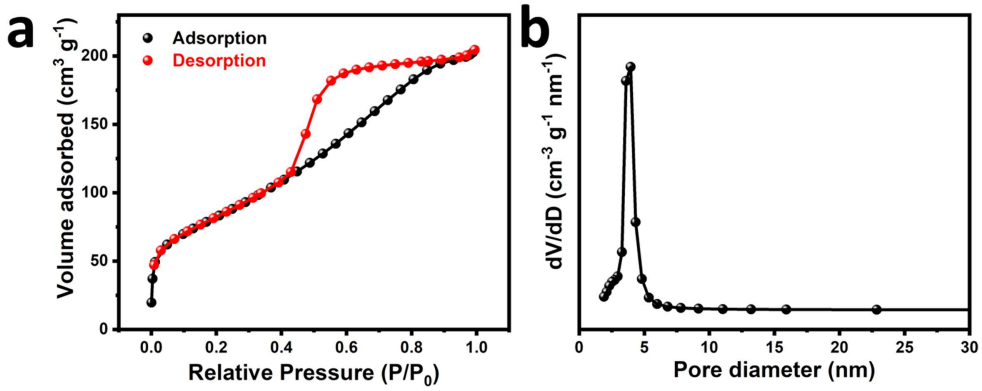

Figure S14 Nitrogen adsorption-desorption isotherms (a) and pore size distribution plot (b) of MnSe-CeO_2@Co_3O_4.

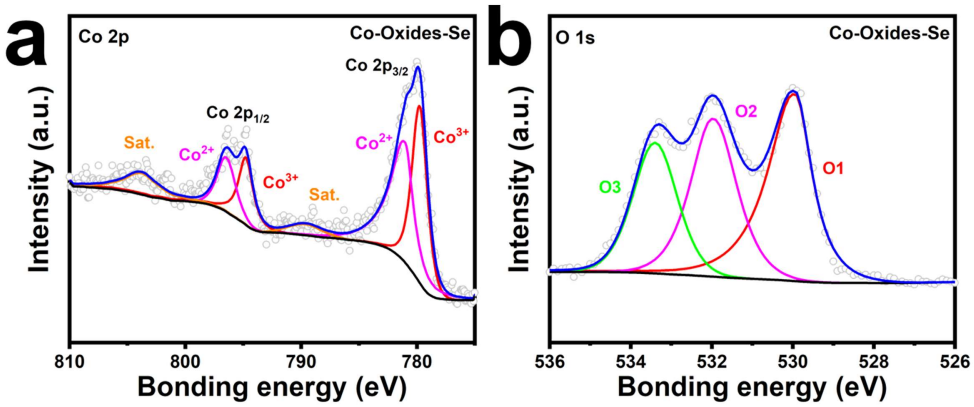

Figure S15 High-resolution XPS spectra of (a) Co 2p and (b) O 1s of Co-Oxides-Se.

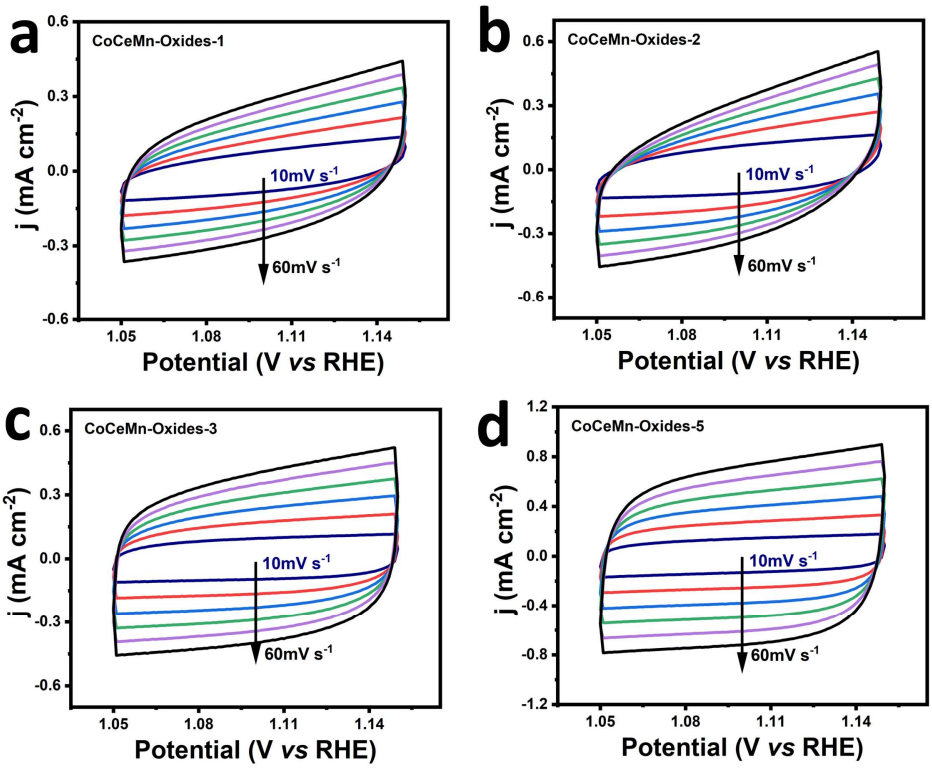

Figure S16 CV curves of (a) CoCeMn-Oxides-1, (b) CoCeMn-Oxides-2, (c) CoCeMn-Oxides-3 and (d) CoCeMn-Oxides-5 with different scan rates from 10 to 60 mV s^{-1}.

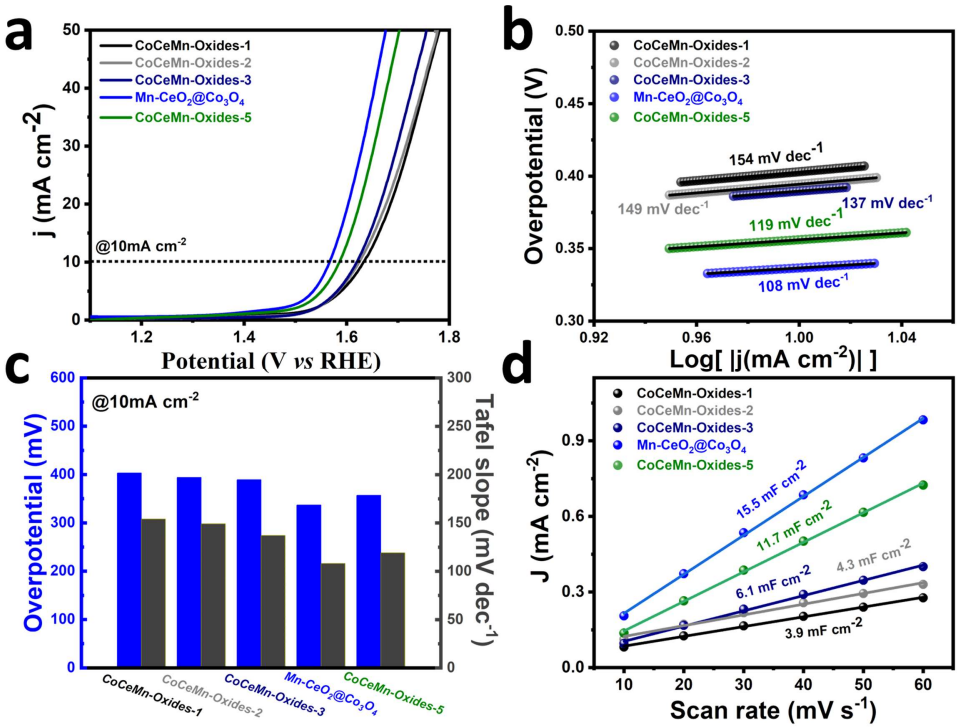

Figure S17 (a) LSV polarization curves of CoCeMn-Oxides-x (x = 1-5) in 1 M KOH aqueous solution for OER. (b) Corresponding Tafel slopes. (c) The corresponding overpotentials and Tafel slopes at 10 mA cm^{-2}. (d) Double-layer capacitance (C_{dl}) obtained by linear fitting of the capacitive currents.

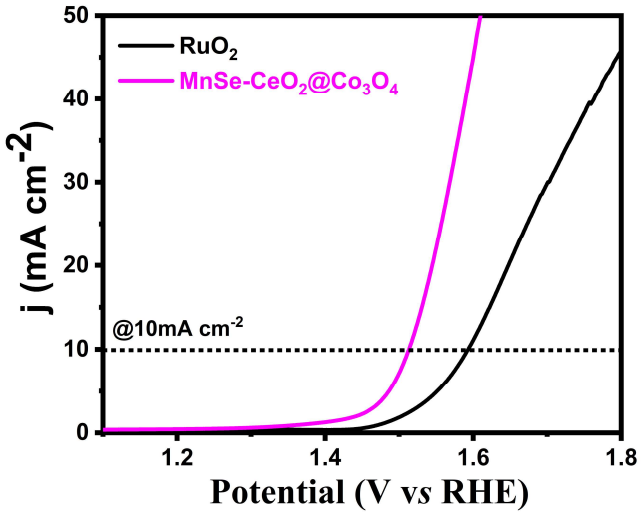

Figure S18 LSV polarization curve of RuO_2 and MnSe-CeO_2@Co_3O_4 in 1 M KOH aqueous solution for OER.

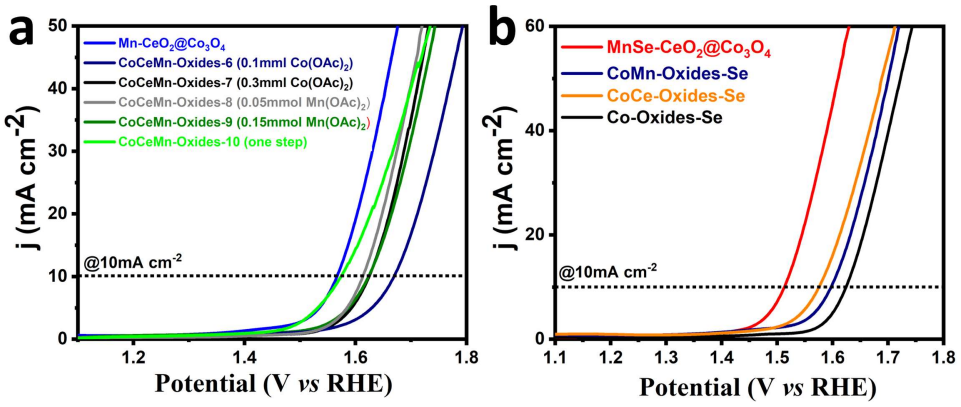

Figure S19 LSV polarization curves of (a) Mn-CeO_2@Co_3O_4, CoCeMn-Oxides-x (x = 6-10) and (b) MnSe-CeO_2@Co_3O_4, CoMn-Oxides-Se, CoCe-Oxides-Se, and Co-Oxides-Se in 1 M KOH aqueous solution.

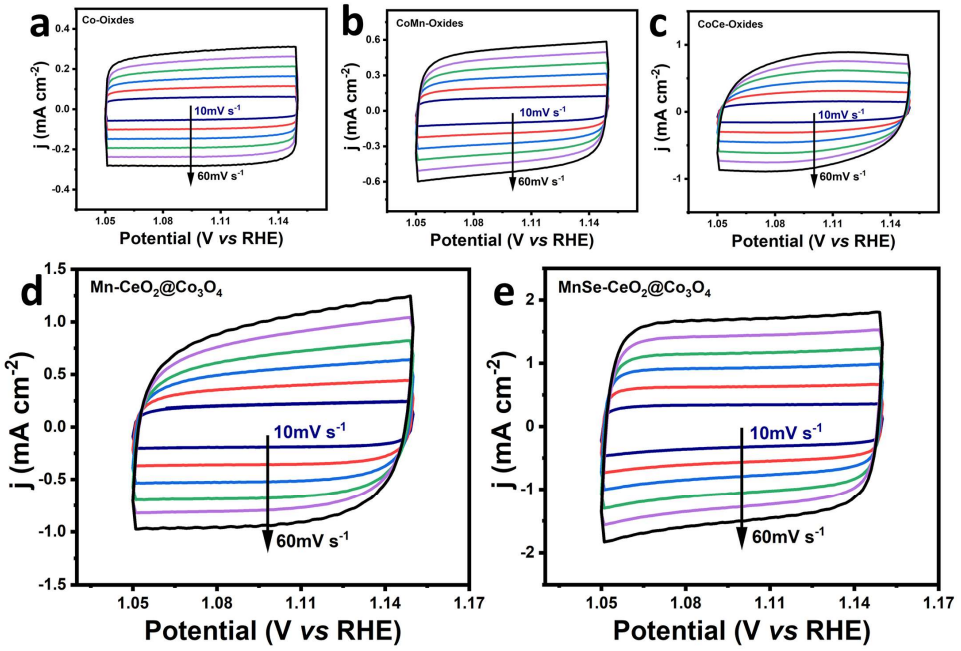

Figure S20 CV curves of (a) Co-Oxides, (b) CoMn-Oxides, (c) CoCe-Oxides, (d) Mn-CeO_2@Co_3O_4 and (e) MnSe-CeO_2@Co_3O_4 with different scan rates from 10 to 60 mV s^{-1}.

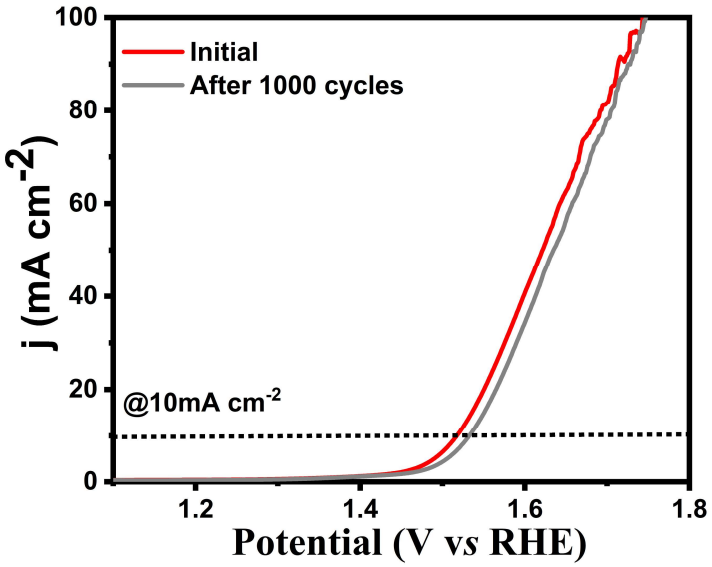

Figure S21 LSV curves of MnSe-CeO_2@Co_3O_4 before and after 1000 cycles of CV test.

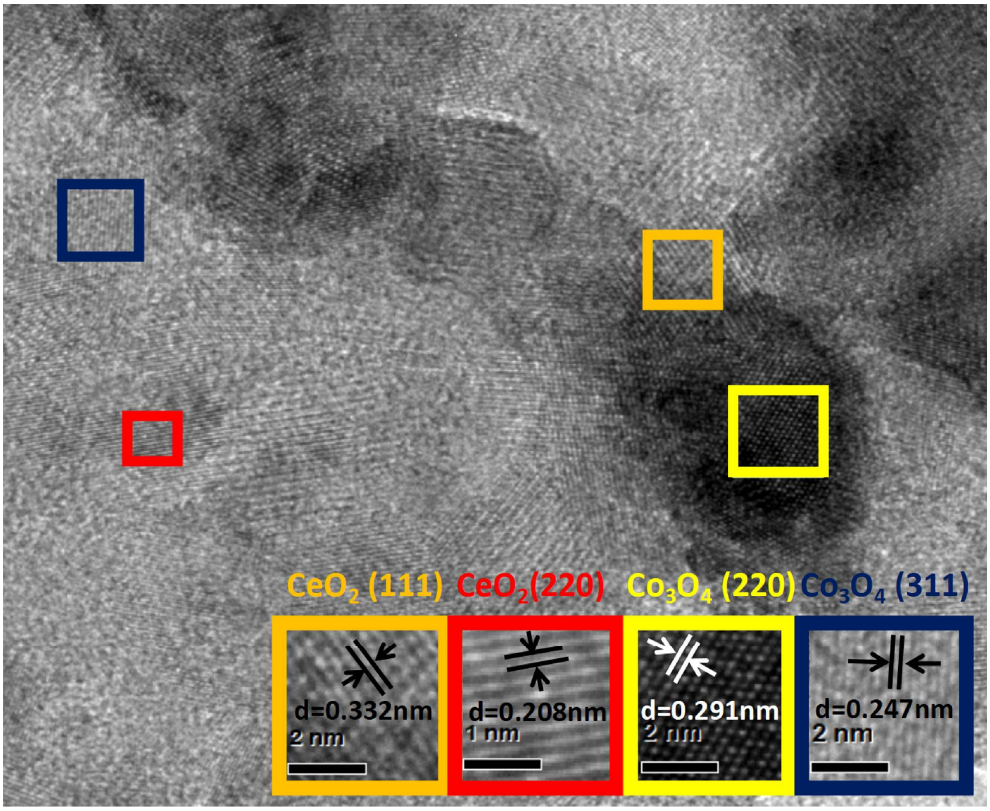

Figure S22 HRTEM image of MnSe-CeO_2@Co_3O_4 after CP test.

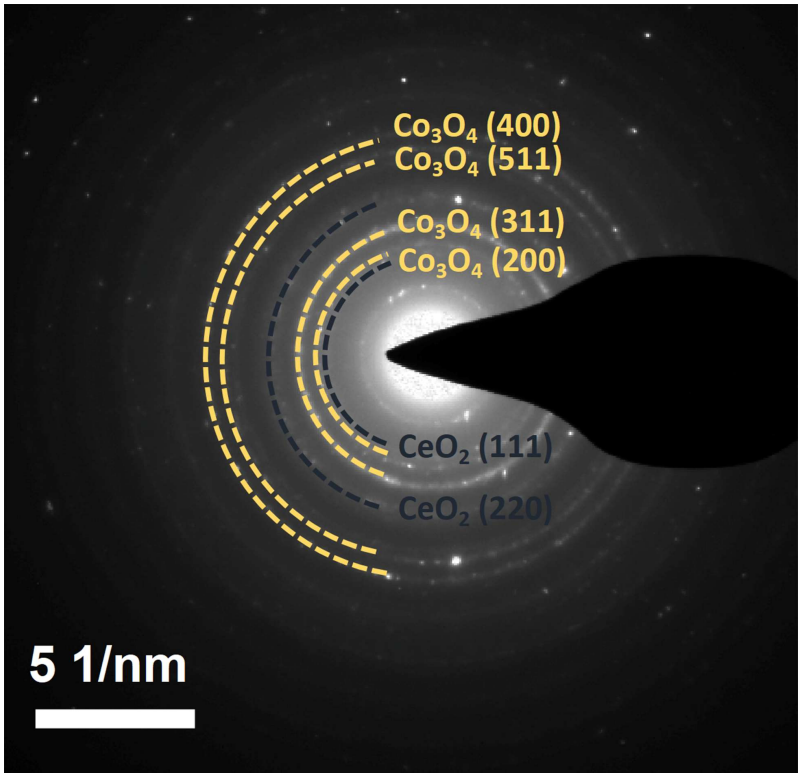

Figure S23 SAED pattern of MnSe-CeO_2@Co_3O_4 after CP test.

Table S1 Atomic ratio of Ce, Co, Mn and Co/Ce from ICP-AES analysis on CoCe-CDSAAs, CoMn-CDSAAs and CoCeMn-CDSAAs-x (x = 1-9).

Samples	Ce (at%)	Co (at%)	Mn (at%)	Co/Ce (atomic ratio)
CoCe-CDSAAs	10.28	89.72	\	8.73
CoMn-CDSAAs	\	90.55	9.45	\
CoCeMn-CDSAAs-1	35.26	61.58	3.16	1.75
CoCeMn-CDSAAs-2	24.57	72.17	3.26	2.94
CoCeMn-CDSAAs-3	17.93	77.89	4.18	4.34
CoCeMn-CDSAAs	9.98	85.26	4.76	8.54
CoCeMn-CDSAAs-5	7.86	86.90	5.24	11.06
CoCeMn-CDSAAs-6	14.56	69.99	15.45	4.81
CoCeMn-CDSAAs-7	6.64	91.65	1.71	13.81
CoCeMn-CDSAAs-8	10.18	86.11	3.71	8.46
CoCeMn-CDSAAs-9	7.94	86.83	5.23	10.94

Table S2 Atomic ratio of Ce, Co, Mn and Co/Ce from EDX analysis on CoCe-Oxides, CoMn-Oxides and CoCeMn-Oxides-x (x = 1-9).

Samples	Ce (at%)	Co (at%)	Mn (at%)	Co/Ce (atomic ratio)
CoCe-Oxides	12.05	87.95	\	7.30
CoMn-Oxides	\	90.71	9.29	\
CoCeMn-Oxides-1	37.42	58.70	3.88	1.57
CoCeMn-Oxides-2	31.51	65.75	2.74	2.08
CoCeMn-Oxides-3	18.36	76.60	5.04	4.17
Mn-CeO_2@Co_3O_4	10.00	84.19	5.81	8.42
CoCeMn-Oxides-5	6.84	86.48	6.68	12.64
CoCeMn-Oxides-6	16.22	66.67	17.11	4.11
CoCeMn-Oxides-7	6.00	92.09	1.91	15.35
CoCeMn-Oxides-8	9.58	85.98	4.44	8.97
CoCeMn-Oxides-9	4.90	89.74	5.36	18.31

Table S3 Atomic ratio of Co^{3+}/Co^{2+} and O2/(O1+O2+O3) from XPS analysis on Co-Oxides, CoMn-Oxides, CoCe-Oxides, Mn-CeO_2@Co_3O_4, MnSe-CeO_2@Co_3O_4, Co-Oxides-Se and MnSe-CeO_2@Co_3O_4 (After CP).

Samples	Co^{3+}/Co^{2+}	O2/(O1+O2+O3)
Co-Oxides	0.66	0.43
CoMn-Oxides	0.79	0.31
CoCe-Oxides	0.41	0.49
Mn-CeO_2@Co_3O_4	0.94	0.45
MnSe-CeO_2@Co_3O_4	1.03	0.37
Co-Oxides-Se	0.94	0.33
MnSe-CeO_2@Co_3O_4 (After CP)	1.06	0.67

Table S4 Comparison of the OER performance of MnSe-CeO_2@Co_3O_4 with previously reported Co_3O_4-based or CeO_2-based OER electrocatalysts in 1M KOH solution.

Catalysts	η (10mA cm^{-2}) (mV)	Reference
MnSe-CeO_2@Co_3O_4	284	This Work
Co-UNMs	307	2
Co_3O_4/NiO@CeO_2-2 HPN	290	3
RuO_2/Co_3O_4 NBs	302	4
Co_3O_4/Co-Fe oxide DSNBs	297	5
Ce-$MnCo_2O_4$-3%	390	6
Ce-Co_3O_4	369	7
1 wt% RuO_2-CeO_2	350	8
3DOM-CC-10	298	9
Mn-Co_3O_4/S	330	10
Co_3O_4/CeO_2@N-CNFs	310	11*
Ru/Ni-Co_3O_4	290	12

* In 0.1M KOH solution.

3 Reference

1 Ge. D, Geng. H, Wang. J. Zheng. J. Pan, Y, Cao. X, Gu. H, Porous Nano-Structured Co_3O_4 Anode Materials Generated from Coordination-Driven Self-Assembled Aggregates for Advanced Lithium Ion Batteries, *Nanoscale*, 2014, **6**, 9689-9694.

2 Li. Y, Li. F, Meng. X, Li. S, Zeng. J., Chen. Y, Ultrathin Co_3O_4 Nanomeshes for the Oxygen Evolution Reaction, *ACS Catal*., 2018, **8**, 1913-1920.

3 Yu. Z, Lin. Y, Gao. X, Guo. B, Ma. J, Zhang. Y, Bai. F, Dong. Y, Zhao. Z, Prussian-Blue-Analog Derived Hollow Co_3O_4/NiO Decorated CeO_2 Nanoparticles for Boosting Oxygen Evolution Reaction, *J. Alloy. Compounds*, 2022, **914**, 165344.

4 Guo. B, Zhang. X, Ma. X, Chen. T, Chen. Y, Wen. M, Qin. J, Nan. J, Chai. Y, Dong. B, RuO_2/Co_3O_4 Nanocubes Based on Ru Ions Impregnation into Prussian Blue Precursor for Oxygen Evolution, *Int. J. Hydrogen Energy*., 2020, **45**, 9575-9582.

5 Wang. X, Yu. L, Guan. B, Song. S, Lou. X, Metal-Organic Framework Hybrid-Assisted Formation of Co_3O_4 /Co-Fe Oxide Double-Shelled Nanoboxes for Enhanced Oxygen Evolution, *Adv Mater*., 2018, **30**, 1801211.

6 Huang. X, Zheng. H, Lu. G, Wang. P, Xing. L, Wang. J, Wang. G, Enhanced Water Splitting Electrocatalysis over $MnCo_2O_4$ via Introduction of Suitable Ce Content, *ACS Sustainable Chem. Eng*., 2018, **7**, 1169-1177.

7 Zhou. J, Zheng. H, Luan. Q, Huang. X, Li. Y, Xi. Z, Lu. G, Xing. L, Li. Y, Improving the Oxygen Evolution Activity of Co_3O_4 by Introducing Ce Species Derived from Ce-Substituted ZIF-67, *Sustainable Energy Fuels*, 2019, **3**, 3201-3207.

8 Galani. S, Mondal. A, Srivastava. D, Panda. A, Development of RuO_2/CeO_2 Heterostructure as an Efficient OER Electrocatalyst for Alkaline Water Splitting, *Int. J. Hydrogen Energy*., 2020, **45**, 18635-18644.

9 Wang. X, Liu. M, Yu. H, Zhang. H, Yan. S, Zhang. C, Liu. S, Oxygen-Deficient 3D-Ordered Multistage Porous Interfacial Catalysts with Enhanced Water Oxidation Performance, *J. Mater. Chem. A*, 2020, **8**, 22886-22892.

10 Qi. J, Wang. H, Lina. J, Li. C, Si. X, Cao. J, Zhong. Z, Feng. J, Mn and S Dual-Doping of MOF-Derived Co_3O_4 Electrode Array Increases the Efficiency of Electrocatalytic Generation of Oxygen, *J. Colloid Interface Sci*., 2019, **557**, 28-33.

11 Li. T, Li. S, Liu. Q, Tian. Y, Zhang. Y, Fu. G, Tang. Y, Hollow Co_3O_4/CeO_2 Heterostructures in Situ Embedded in N-Doped Carbon Nanofibers Enable Outstanding Oxygen Evolution, *ACS Sustainable Chem. Eng*., 2019, **7**, 17950-17957.

12 Guo. B, Ma. R, Li. Z, Luo. J, Yang. M, Wang. J, Dual-Doping of Ruthenium and Nickel into Co_3O_4 for Improving the Oxygen Evolution Activity, *Mater. Chem. Front*., 2020, **4**, 1390-1396.